 doi:10.20944/preprints201912.0408.v1

Article

A tri-band low-noise cryogenic receiver for geodetic VLBI observations with VGOS radio telescopes

José A. López-Pérez, Félix Tercero-Martínez, José M. Serna-Puente, Beatriz Vaquero-Jiménez, María Patino-Esteban, Pablo García-Carreño, Javier González-García, Óscar García-Pérez, Francisco J. Beltrán-Martínez, Carlos Albo-Castaño, Juan D. Gallego-Puyol, Isaac López-Fernández, Carmen Díez-González, Inmaculada Malo-Gómez, Laura Barbas-Calvo, Pablo de Vicente-Abad, José A. López-Fernández

[1] Yebes Observatory, Centro de Desarrollos Tecnológicos, Instituto Geográfico Nacional, Ministerio de Fomento, Cerro de la Palera s.n., Yebes, E-19141, Guadalajara, SPAIN; ja.lopezperez@oan.es

* Correspondence: ja.lopezperez@oan.es; Tel.: +34-949-29-03-11

Abstract: This paper shows the development of a simultaneous tri-band (S: 2.2 - 2.7 GHz, X: 7.5 - 9 GHz and Ka: 28 - 33 GHz) low-noise cryogenic receiver for geodetic Very Long Baseline Interferometry (geo-VLBI) which has been developed by the technical staff of Yebes Observatory laboratories in Spain. The receiver was installed in the first radio telescope of the *Red Atlántica de Estaciones Geodinámicas y Espaciales* (RAEGE) project, which is located in Yebes Observatory, in the frame of the VLBI Global Observing System (VGOS). After this, the receiver was borrowed by the Norwegian Mapping Autorithy (NMA) for the commissioning of two VGOS radiotelescopes in Svalbard (Norway). A second identical receiver was built for the Ishioka VGOS station of the Geospatial Information Authority (GSI) of Japan, and a third one for the second RAEGE VGOS station, located in Santa María (Açores Archipelago, Portugal). The average receiver noise temperatures are 21, 23 and 25 Kelvin and the measured antenna efficiencies are 70%, 75% and 60% in S-band, X-band and Ka-band, respectively.

Keywords: VLBI; Geodesy; Radioastronomy; Radiotelescope; Receiver; Radiometer; Feed; Backend; Correlation; VGOS; RFI

1. Introduction

The Yebes Observatory of the Spanish *Instituto Geográfico Nacional* (IGN) has developed a simultaneous tri-band (S/X/Ka) low-noise cryogenic receiver for geodetic VLBI observations with VGOS-type radiotelescopes [1], as the ring-focus antennas of the RAEGE network project [2].

This receiver operates in the S (2.2 - 2.7 GHz), X (7.5 - 9 GHz) and Ka (28 - 33 GHz) bands, simultaneously, in order to be backward compatible with legacy VLBI stations and forward compatible with X/Ka VLBI ones.

The receiver feed was designed to illuminate the ring focus antenna and is made of a coaxial waveguide, for the S and X bands, and a circular waveguide for the Ka band. Four outputs, from their corresponding field probes at S and X bands, must be combined with 180° and 90° hybrid circuits to get simultaneous dual-circular polarization. In the Ka-band case, the two circular polarizations are splitted by means of a classical septum polarizer/coupler. The feed, hybrids and polarizer will operate at cryogenic temperature in order to minimize their contribution to receiver noise.

The measured average equivalent noise temperature for this receiver is 21 Kelvin for S-band, 23 Kelvin for X-band and 25 Kelvin for Ka-band.

The output signals from the cryostat are sent to their corresponding room temperature downconverters for later amplification, filtering and mixing. The final IF signal ranges from 500 to 1000 MHz, in S and Ka bands, and from 100 to 1000 MHz in X-band, as in classical geodetic VLBI receivers, to be backward compatible with older stations.

Preprints (www.preprints.org) | NOT PEER-REVIEWED | Posted: 31 December 2019 doi:10.20944/preprints201912.0408.v1

Figure 1. Yebes VGOS 13.2 meter radio telescope

An advantage of having the Ka-band receiver is that it allows the radiometric characterization (pointing, tracking and efficiency) of these radiotelescopes during commissioning. In addition, simultaneous X/Ka operation is feasible for astrometric observations, too.

Three of these receivers were built in Yebes laboratories. The first one was in operation in the Yebes 13.2 m RAEGE radio telescope (see figure 1), until it was exchanged by a broad-band VGOS receiver (2-14 GHz). It is now borrowed by the Norwegian Mapping Authority (NMA) for the commissining of the Ny-Alesund radiotelescopes in Svalbard. The second one was developd for the 13.2 m VGOS antenna of the Geospatial Information Authority (GSI) in Japan. Finally, the third one is installed in the 13.2 m RAEGE antenna in Santa María (Açores archipelago, Portugal).

The main advantages of this receiver are the following:

- Simultaneous S/X/Ka reception.
- Simultaneous dual circular polarization is obtained and there is no need to perform operations on digitized data to retrieve circular polarizations from linear ones.
- Backward compatible with legacy VLBI stations and forward compatible with X/Ka VLBI ones.
- Reduced feed size for cooling down to 15 Kelvin, minimizing the feed noise contribution.
- Traditional cryogenic low-noise amplifier (LNA) design versus differential one.
- Ease of calibration signal injection (NoiseCal and PhaseCal) in front of LNA's.
- Less sensitive to radio frequency interferences (RFI) than broadband systems (VGOS), which need protection circuits at the input of their LNA's.
- Ka-band receiver allows accurate radiometric characterization of telescope pointing, tracking and gain at high frequencies for antenna commisioning.

However, the major drawbacks are:

- The 180° and 90° microwave hybrid couplers are needed in S and X bands to combine the signals from the feed ports. In addition, they must operate at 20 Kelvin to minimize their contribution to receiver noise. However, a cryogenic 90° hybrid has been developed in house with very good properties. For the 180° ones, commercial units have been purchased and successfully tested at cryogenic temperatures without substantial degradation of their performance.
- The receiver has not a coverage of the 2-14 GHz band, as requested by VGOS project specifications.

 doi:10.20944/preprints201912.0408.v1

2. The tri-band receiver

For the first light of the first RAEGE radio telescope, in Yebes Observatory, it was decided to develop a tri-band receiver because it can assure compatibility with legacy VLBI stations, in S/X bands, and the Ka-band receiver allows the high frequency characterization of the telescope during commissioning [3]. This section shows the design of this receiver and its subsystems.

The receiver requirements were the following:

- Simultaneous S/X/Ka band reception
- S-band range: 2.2 - 2.7 GHz
- X-band range: 7.5 - 9 GHz
- Ka-band range: 28 - 33 GHz
- Simultaneous dual circular polarization in all bands
- Mean receiver noise temperature < 30 Kelvin
- NoiseCal and PhaseCal injection
- Cooled receiver feed
- Cooling time < 12 hours

2.1. Receiver Block Diagram

The full tri-band receiving system is depicted in figure 2. The following modules can be seen:

- The cryostat (dewar) with the feed horn, couplers and low noise amplifiers inside to be cooled down to 15 Kelvin.
- S-band downconverter
- X-band downconverter
- Ka-band downconverter
- RF-over-fiber optical transmitter for IF signal transportation to the optical receivers and VLBI backends in the 40 meter radio telescope backend room. This transportation is performed through a 420 meter length fiber optic cable.
- NoiseCal and Phasecal Antenna Unit, for calibration signals generation
- 5MHz distributor to feed tri-band downconverters with the reference frequency signal.
- PhaseCal Ground Unit in the 13.2 meter radio telescope pedestal, which is fed by 5MHz signal brought from the 40 meter backend room through optic fiber link, as well as the 80 Hz signal for continuous amplitude calibration by switching of the noise diode in the NoiseCal module. This signal is not required for geodetic VLBI, but it was needed for the ease of receiver calibration.

The following sections will provide a detailed description of each module.

2.2. Receiver Feed

The VGOS specifications require broad-band operation of the receiver from 2 to 14 GHz. There are several feeds to be used as a broad-band feed in VGOS project [4] [5] [6] [7]. All these feeds have different types of output polarization (simultaneous linear and circular) and different types of output interfaces to the low noise amplifier (single-ended and differential). However, what it is relevant from the antenna design view point, is that all these feeds have a similar f/D range of operation (f/D=0.3), broad beamwidth and low directivity. This characteristic is important to define the dual reflector antenna, because it is unusual to have such a low f/D in dual reflector design, due to the fact that they show high blockage inefficiencies. To solve this issue, the ring-focus design avoids the blockage both from the feed and the subreflector when feeds with low f/D are used. Figure 3 shows the profiles of the RAEGE 13.2 meter radio telescope.

As a consequence, the feed to be designed must illuminate with a -16 dB taper for the 65^o semiangle at the edge of the subreflector. Phase centre of the feed must be coincident with the secondary focus of the antenna.

Preprints (www.preprints.org) | NOT PEER-REVIEWED | Posted: 31 December 2019 doi:10.20944/preprints201912.0408.v1

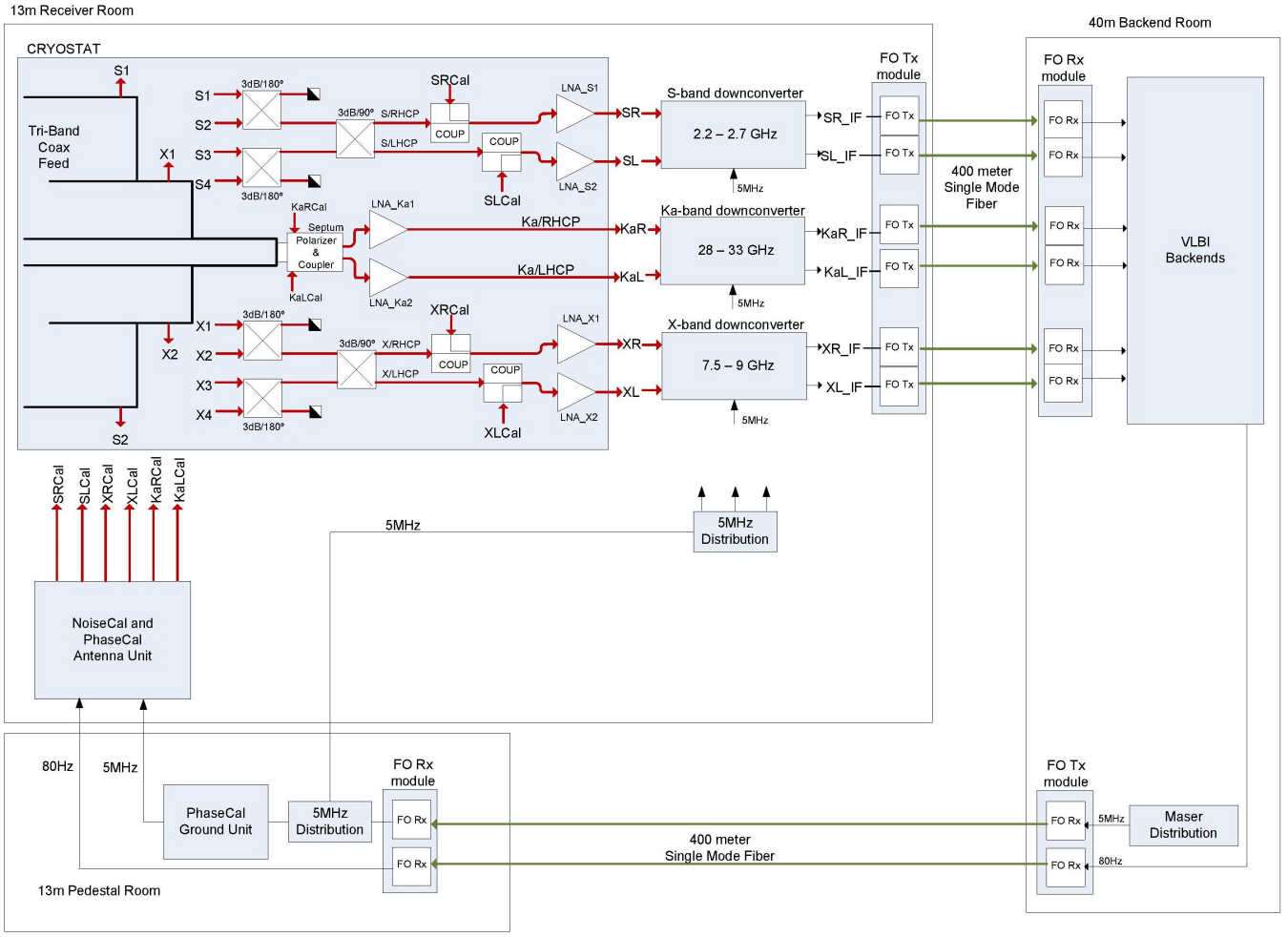

Figure 2. Tri-band receiver block diagram.

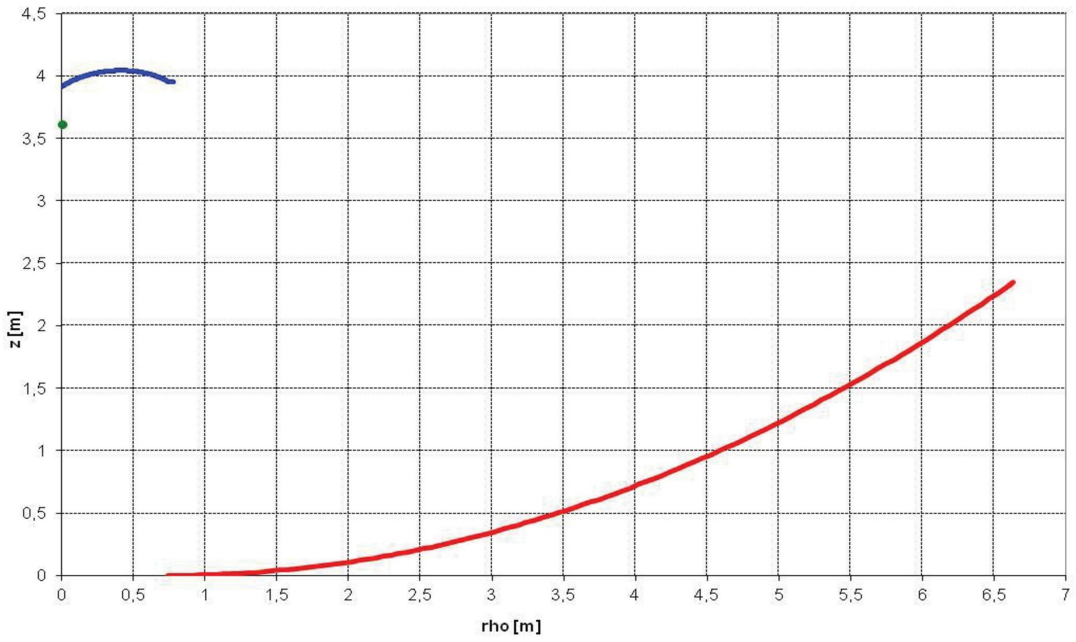

Figure 3. RAEGE radio telescope reflector profile.

Preprints (www.preprints.org) | NOT PEER-REVIEWED | Posted: 31 December 2019 doi:10.20944/preprints201912.0408.v1

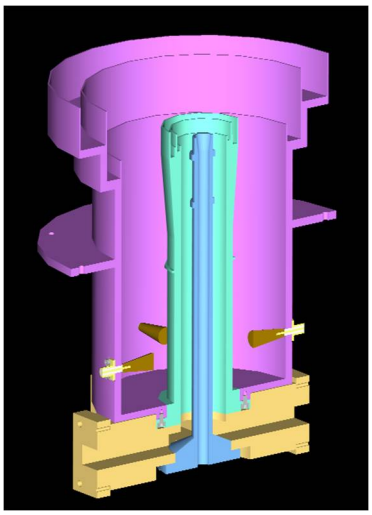

Figure 4. Internal view of Tri-band receiver feed.

The tri-band receiver feed, which is shown in figure 4 has been designed to illuminate the ring-focus antenna. It is made of a coaxial waveguide, for the S and X bands, and a circular waveguide for the Ka band. The biggest coaxial waveguide is the S-band one, whose inner conductor acts as the external one of the X-band waveguide. The same structure, with smaller dimensions, is repeated for the X band. In this case the inner coaxial conductor is the exterior one of the Ka-band. Finally, the smallest feed near to the axial axis is the Ka-band one, which is a single smooth conical feed. As the three feeds have the same beam-width, their apertures are scaled with the frequency. This fact makes possible the tri-band operation. The feed dimensions are 25 cm high and 20 cm in diameter and it weights 3 Kg.

The three horns have independent outputs. In the case of the S-band coaxial horn, 4 coaxial field probes are combined to get dual-circular polarization. Opposite probes are combined in a 180° hybrid coupler to get one linear polarization. Both linear polarizations are then combined in a 90° hybrid coupler (see details in section 2.4) to get dual circular polarization. For the X-band coaxial horn, similar layout is used but standard WR-112 to SMA-coaxial transitions are used. Then, 180° and 90° hybrid couplers are used the same way, to transform linear to circular polarizations. Since the 180° and 90° hybrids are connected with coaxial cables, they were phased matched to have the same electrical length, resulting in a low axial ratio in circular polarization. For the Ka-band feed, the output is a circular waveguide with 8.4 mm in diameter. It is directly attached to a septum polarizer which provides dual circular polarization in 2.92 mm coaxial connectors. This polarizer device includes a coupler for injection of noise and phase calibration signals.

The septum polarizer can be seen in figure 5, where lateral coaxial connectors are for RCP and LCP outputs and front coaxial connectors are for calibration signal injection into the RCP and LCP chains. The circular waveguide port (top) connects to the Ka-band feed.

The tri-band feed radiation patterns were simulated using Ansys HFSS software. The feed was built and measured in the Yebes Observatory's anechoic chamber. Figure 6 shows the measured radiation patterns at 2.4, 8 and 33 GHz, where a constant beam-width in the three bands to illuminate the ring reflector can be seen.

2.3. Receiver Cryostat

The cryostat is built over a two-stage Sumitomo closed-cycle refrigerator (SHI RDK-408S2, Gifford-McMahon cryocooler) inside a stainless steel cylindrical dewar. The selection of this cryocooler was made after a complete analysis of the thermal loads in the cryostat due to gas conduction, solid conduction, radiation and power dissipation of electronic devices (cryogenic low-noise amplifiers).

Preprints (www.preprints.org) | NOT PEER-REVIEWED | Posted: 31 December 2019 doi:10.20944/preprints201912.0408.v1

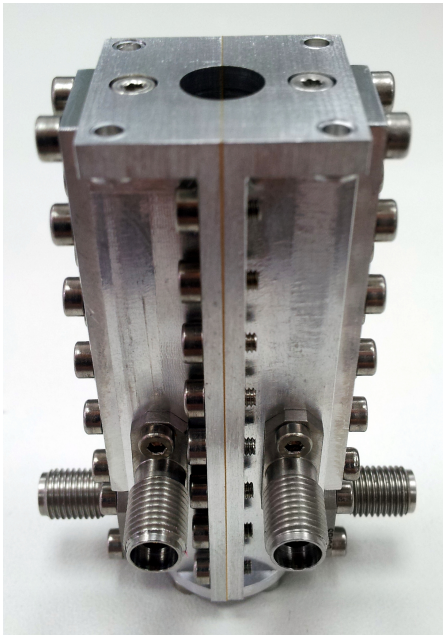

Figure 5. Ka-band septum polarizer and coupler.

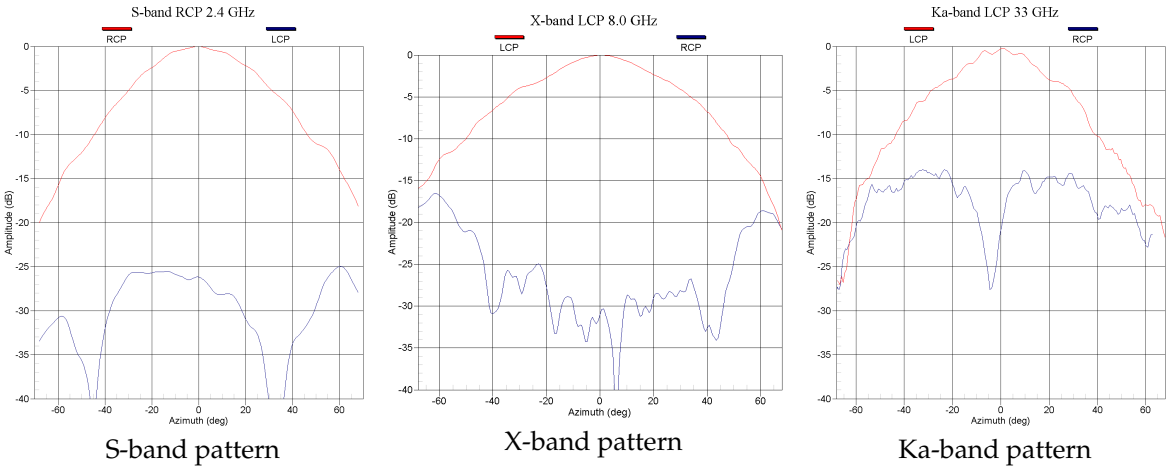

Figure 6. Measured radiation patterns of the tri-band feed in S, X and Ka bands.

Preprints (www.preprints.org) | NOT PEER-REVIEWED | Posted: 31 December 2019 doi:10.20944/preprints201912.0408.v1

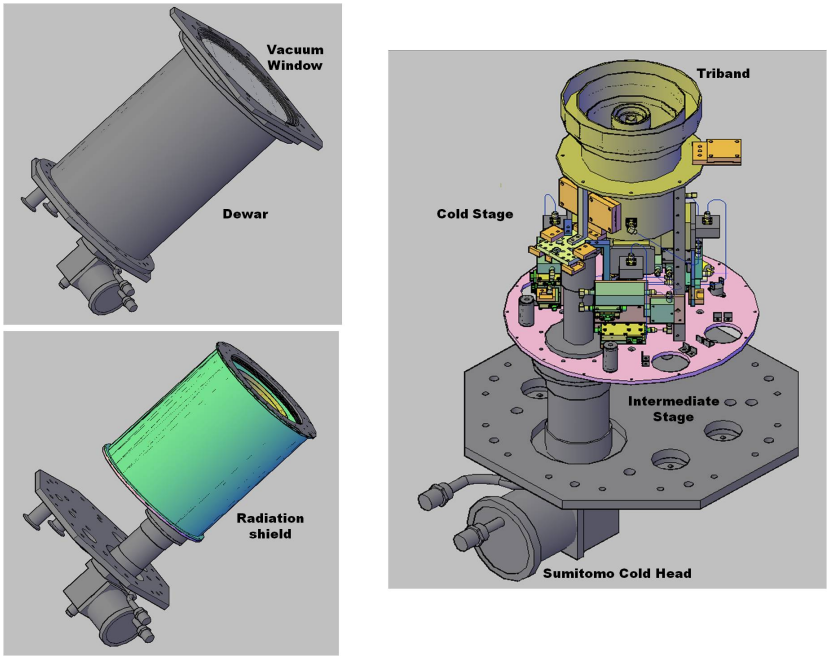

Figure 7. Cryostat design.

The dewar itself consists of three main parts: stainless steel enclosure, aluminum bottom flange and top flange. These parts can be seen in figure 7.

The vacuum window for the microwave signal input is located at the top flange. Its purpose is to allow the transmision of eletromagnetic waves to the triband feed while keeping the vacuum conditions inside the dewar. For this receiver, the vacuum window is made of Mylar.

The dewar bottom flange has several interfaces for the following purposes:

- Connection of the cryocooler cold head.
- Two openings with a transition for vacuum control and monitoring (pressure sensor and vacuum valve, respectively).
- Hermetic Fischer connectors for housekeeping control and monitoring and biasing of low-noise amplifiers.
- SMA and K hermetic coaxial connectors for the injection of amplitude and phase calibration signals and extraction of RF signals after low-noise amplification.

Inside the cryostat, there is an aluminum tube, named radiation shield, that covers the cold stage and reduce the thermal radiation load on it. It is mirror polished to reduce its emissivity and screwed to the intermediate stage, which is an aluminum plate screwed onto the first cooling stage of the cryocooler. In order to improve the efficiency of the radiation shield, it is covered with a multi-layer isolator (MLI) made of Mylar layers. Finally, on top of the radiation shield, an infrared filter is installed to minimize the thermal load due to infrared radiation coming from the outside of the cryostat through the vacuum window towards the cold stage.

On the intermediate stage, some housekeeping devices like temperature sensors (silicon diodes), heating resistors, a thermostat and zeolites-based vacuum traps are placed. These devices allow to achieve a better vacuum level inside the cryostat and to warm up the dewar very fast, if needed for maintenance.

All the front-end has been assembled over a fibre glass composite skeleton that holds the different receiver components: tri-band feed, 180° and 90° hybrid circuits, couplers for injection calibration signals, microwave isolators and S/X cryogenic low-noise amplifiers. The Ka-band septum-type polarizer/coupler and low-noise amplifiers are attached directly to the Ka-band feed.

Preprints (www.preprints.org) | NOT PEER-REVIEWED | Posted: 31 December 2019 doi:10.20944/preprints201912.0408.v1

Figure 8. Receiver components inside de cryostat.

Over the fibre glass skeleton, the feed and all the passive components positions were carefully mechanically designed to keep good symmetry. It was a must to keep the same distance between the feed outputs and the hybrid inputs and have the same cable distance. Otherwise, the different cable length could mess up with the axial ratio performance of the feed.

The cold stage consists of a copper plate screwed onto the second stage of the cryocooler. Copper braids and indium sheets are used to improve the thermal connection between the cold stage and the receiver components. In addition, all the surfaces attached to the cryocooler cold stage are polished to reduce their emissivity.

Finally, all the RF cabling is made of coaxial semi-rigid and hand-formable copper cable in the cold stage. The cables that connect the cold stage with the room temperature stage (bottom flange) are made of semi-rigid stainless-steel coaxial cable in order to minimize the conducted thermal load. For the DC connections (LNAs biasing signals, temperature sensors, heating resistors and vacuum traps regeneration resistors), phosphor bronze thin cross-section wire with very low thermal conductivity was used. Figure 8 shows the receiver components inside the cryostat from two different angles.

In order to characterize the vacuum and thermal behaviour of the cryostat, a set of measurements was performed. For instance, figure 9 shows the time evolution of the temperature of tri-band feed, intermediate and cold stages during a cooling and warming cycle.

Table 1 summarizes the results of these measurements.

Parameter	**Value**
Intermediate stage temperature	< 33 Kelvin
Cold stage temperature	< 16 Kelvin
Tri-band feed temperature	< 9 Kelvin
Vacuum pressure	$< 10^{-5}$ mbar
Leakage rate	$< 1.8 \cdot 10^{-5}$ mbar/s
Cooling time	< 11 hours
Warming time with heaters	< 11 hours
Warming time without heaters	< 23 hours

Table 1. Cryostat performance.

Preprints (www.preprints.org) | NOT PEER-REVIEWED | Posted: 31 December 2019 doi:10.20944/preprints201912.0408.v1

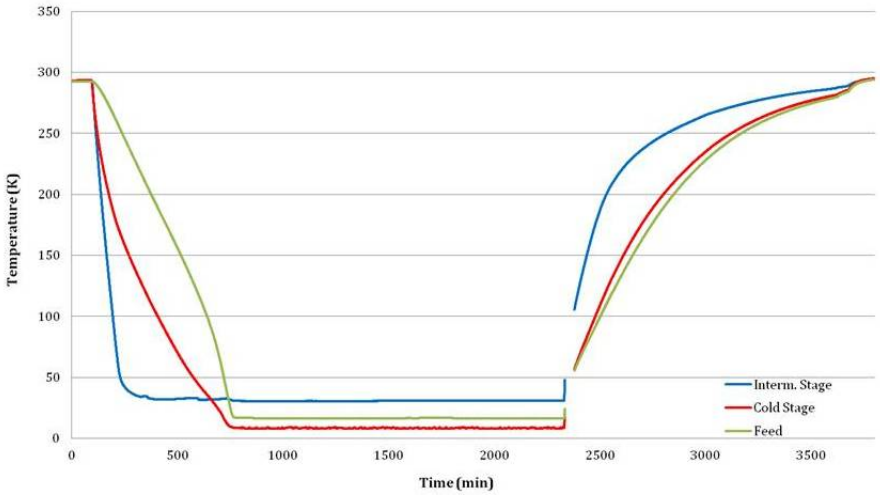

Figure 9. Time evolution of temperatures inside the cryostat.

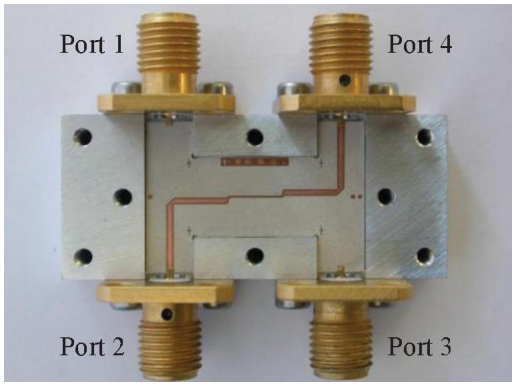

Figure 10. Partly assembled coupler. The picture shows one half of the coupler (without the separation Mylar sheet), the aluminum chassis and the SMA connectors.

2.4. Hybrid Circuits

As shown in the block diagram (figure 2), the receiver needs three cryogenic hybrid couplers for each band (S and X) to combine the signals from the feed probes (90° apart) to get the two ortogonal circular polarization signals, as requested by VLBI correlators. Two of these couplers are 3 dB 180° hybrids, while the third one is 3 dB 90° hybrid.

The 3 dB 180° hybrids are commercial off-the-shelf units which have been tested a cryogenic temperatures with successful results. However, the 3 dB 90° hybrids have been designed in Yebes laboratories [8], and they are particularly designed for operation at 15 Kelvin.

The design of the 3 dB 90° hybrids couplers is based in a coupled line structure in stripline technology in order to achieve strong couplings in a multioctave bandwidth. Specifically, an offset broadside coupled stripline, with a dielectric separation layer (see figure 10).

In a wide bandwidth design, it is necessary to use a three-quarter-wavelength coupler [9], so the coupling will have an adequate ripple in the whole band. The materials and mechanical construction have been carefully selected. The hybrid must operate at 15 Kelvin without degradation; therefore all the materials used in the manufacturing process should have a high thermal stability. The most critical parameter in the design is the separation between the substrates of the stripline because it strongly affects the coupling factor. Similar thermal expansion coefficient in the Z axis of the chassis and substrate keeps this separation stable when cooling. In addition, a thin separation layer of Mylar is introduced between the substrates, with higher rigidity and superior thermal stability than other similar polymers, and a permittivity very similar to the substrate. A very important practical problem

Preprints (www.preprints.org) | NOT PEER-REVIEWED | Posted: 31 December 2019 doi:10.20944/preprints201912.0408.v1

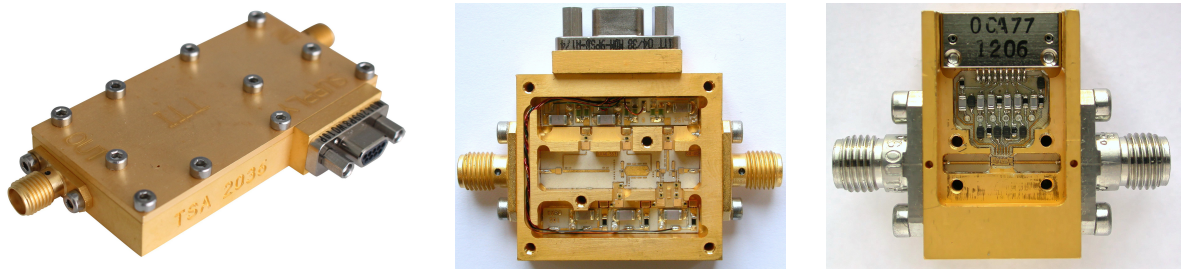

S-band LNA X-band LNA Ka-band LNA

Figure 11. Cryogenic low noise amplifiers for the tri-band feed in S, X and Ka bands.

is the reliability of the contact between the substrates and the input/output connectors. Commercial hybrids use standard SMA connectors directly soldered to the substrates. The mechanical stress produced by the variation of temperature, from 300 to 15 Kelvin, can easily lead to failures in the solder joints, after repeated thermal cycles. To minimize this risk, connectors with sliding central pin has been used, as they allow slight shifts of the central pin alleviating the mechanical stress. The pins were glued with conductive epoxy to the circuit lines.

The resulting hybrids are very compact, low-loss, reliable, repetitive and low thermal mass devices, capable to withstand extreme thermal cycling. Their coupling and reflection characteristics show very little temperature dependence.

An example of the performance of a 3 dB 90° hybrid coupler for X-band is shown in table 2, where the average equivalent insertion loss is given by $L_{eq} = 10log_{10}(|S_{11}|^2 + S_{12}|^2 + S_{13}|^2 + S_{14}|^2)$.

Serial Number	**YH90X 1019**	
Description	3 dB 90° cryogenic hybrid	
Frequency range	4 - 12 GHz	
Nominal coupling	3 dB	
Connector	SMA female, sliding pin	
Weight (typ.)	< 36 g (1.27 oz)	
Temperature	297 Kelvin	20 Kelvin
Average equivalent insertion loss, L_{eq}	0.55 dB max	0.21 dB max
Max. return loss (any port)	-19 dB	-17.9 dB
Amplitude unbalance (max)	±0.27 dB	±0.3 dB
Phase unbalance (max)	$\pm 2^o$	$\pm 2.3^o$

Table 2. X-band 3 dB 90° hybrid coupler performance.

2.5. Low-Noise Amplifiers

The cryogenic low noise amplifiers (LNAs) are key elements in defining the overall sensitivity of receivers, particularly in the current frequency range, for which direct amplification of the sky signal is possible. Yebes Observatory has a long tradition in the design and manufacturing of state-of-the-art reliable cryogenic amplifiers based on heterojunction field-effect transistor (HFET) devices.

The following subsections will show the performance of each set of low noise amplifiers, which are shown in figure 11.

All amplifiers units were characterized at cryogenic temperature in the closed-cycle helium dewars of Yebes laboratories. Noise performance was measured using the cold attenuator method as described in [14]. The cryogenic attenuator of the Ka-band test set is a special design which allows an efficient cooling of the resistive elements and an accurate reading of its temperature, minimizing the effect of the stray heating produced by the inner conductor of the input coaxial cable. An absolute

Preprints (www.preprints.org) | NOT PEER-REVIEWED | Posted: 31 December 2019 doi:10.20944/preprints201912.0408.v1

accuracy (2σ) at ambient temperature (T_{amb} = 14 Kelvin) of 2.8 Kelvin for a typical Ka-band amplifier and of 1.4 Kelvin for a typical X-band amplifier can be estimated with methods presented in [15]. Repeatability is better than these values by an order of magnitude.

S-parameters were measured with a vector network analyzer (VNA). The effect of the dewar hermetic transitions and stainless steel access lines is de-embedded. The change with temperature of the cryogenic cable at the DUT output is also taken into account. The small variations of the transitions upon cooling are corrected by using time domain gating. The amplifiers were also extensively tested to confirm the absence of spurious out-of-band oscillations around the nominal bias settings.

Plots with the noise and gain measurements at cryogenic temperature are shown in figures 12, 13 and 14. A summary of the performance of the three designs is presented in table 3.

Frequency range (GHz)	2.2 - 2.7	7.5 - 9	28 - 33
Power dissipation (mW)	5.2	8.3	7.1
Average noise temperature (Kelvin)	3.4	5.5	16.4
Average gain (dB)	26.2	33.6	24.9
Gain flatness (dBpp)	0.7	0.4	0.5
Max. input return loss (dB)	-11	-3.3	-9.5
Max. output return loss (dB)	-16	-12.8	-12.3

Table 3. Typical performance of tri-band receiver LNAs.

2.5.1. S-band low noise amplifiers

S-band amplifiers were manufactured by the Spanish company TTI[1]. The design is a legacy of the LNAs built for the low IF bands of HIFI[2], from 2.4 to 4.8 GHz, which were used for the receivers with HEB mixers [10]. It was tuned in the 2.2 - 2.7 GHz frequency range and optimized for the mechanical and electrical requirements of the tri-band receiver. The amplifiers are implemented in hybrid technology. They include two stages with InP TRW[3] HFETs (100 nm gates) developed for the CHOP[4] project.

The gain and noise temperature of these amplifiers is shown in figure 12.

2.5.2. X-band low noise amplifiers

X.band amplifiers benefited from the very successful design [11] made at Yebes Observatory for the cryogenic low noise amplifiers of ALMA[5] band 9. The bandwidth required by the tri-band receiver (7.5 - 9 GHz) is narrower than the nominal band of those amplifiers (4 - 12 GHz). However, their performance is similar to narrowband designs in the VLBI/DSN X-band (8 - 9 GHz) [12]. The only drawback of this wideband approach is the need of an input isolator, as it is not optimized for low input reflection. The cryogenic isolators used here were manufactured by PAMTECH[6]. They guarantee an optimal matching; however, this poses a penalty of about 1 Kelvin in noise temperature and increases the complexity of the receiver.

The X-band LNAs manufactured for the tri-band receiver were not different to the units delivered to ALMA. It is an hybrid design in microstrip technology with three stages of InP HFETs from HRL[7] (lattice matched 100 nm gate technology) in common source. The matching networks are implemented

---

1 TTI Norte, Spain; www.ttinorte.com.
2 HIFI is the Heterodyne Instrument for the Far-Infrared, onboard the European Space Agency Herschel Observatory.
3 Formerly TRW, now a part of Northrop Grumman Corp.
4 Cryogenic HEMT Optimization Program initiated by NASA/JPL with the participation of Yebes Observatory.
5 ALMA, the Atacama Large Millimeter Array.
6 PAMTECH Inc. is now a division of Quinstar Technology Inc.
7 Hughes Research Labs.

Preprints (www.preprints.org) | NOT PEER-REVIEWED | Posted: 31 December 2019 doi:10.20944/preprints201912.0408.v1

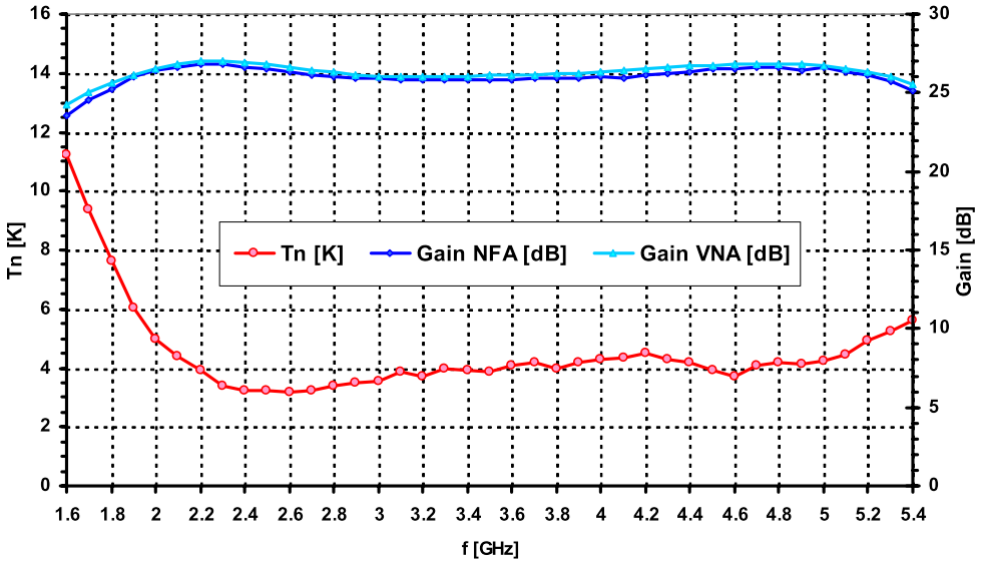

Figure 12. Gain and noise temperature plots of the S-band LNA at 14 Kelvin ambient temperature.

in a soft substrate suitable for operation at cryogenic temperature. The input matching circuit is optimized for noise, while the interstages are tuned for gain flatness and the output circuit for output reflection. Each transistor is independently stabilized by source inductive feedback and drain resistive loading. The bias networks comprise RC filtering sections, which are mounted on the chassis, and also protect the sensitive InP devices from ESD by means of a voltage divider and a charge divider.

The gain and noise temperature of these amplifiers is shown in figure 13.

2.5.3. Ka-band low noise amplifiers

Ka-band amplifiers are one of the outcomes of a collaboration agreement between the IAF[8] the UC[9] and Yebes Observatory. Within this framework, a 2.5 x 1 mm MMIC was designed in the 25 - 34 GHz band with the aim of covering the needs of the radio astronomy and geodesy community, as well as the up and down links of the deep space communication antennas [13]. It is a design in coplanar waveguide technology with three stages of HFETs profiting from the excellent metamorphic GaAs 100 nm process of IAF, competitive with InP analogs.

The MMIC is packaged in a gold plated aluminum module similar to the ones used for the other bands, with 50 ohms microstrip access lines in soft substrates. Part of the biasing networks are embedded in the MMIC. ESD protection is achieved with SMD diodes and high value capacitors in a PCB attached to the module. Although the amplifier is used in the tri-band receiver with coaxial ports (2.92 mm connectors), it is prepared to exchange these connectors by coaxial to waveguide transitions. The noise temperature of the LNA improves 1 to 2 Kelvin in this configuration.

The gain and noise temperature of these amplifiers is shown in figure 14.

2.6. Frequency Downconverters

This sections shows the design, integration and characterization of the three dual-channel downconverters for the tri-band receiver. Table 4 shows a summary of the downconverter properties, as measured in the laboratory.

---

[8] Fraunhofer Institute for Applied Solid StatePhysics, Freiburg, Germany.
[9] Universidad de Cantabria, Spain.

Preprints (www.preprints.org) | NOT PEER-REVIEWED | Posted: 31 December 2019 doi:10.20944/preprints201912.0408.v1

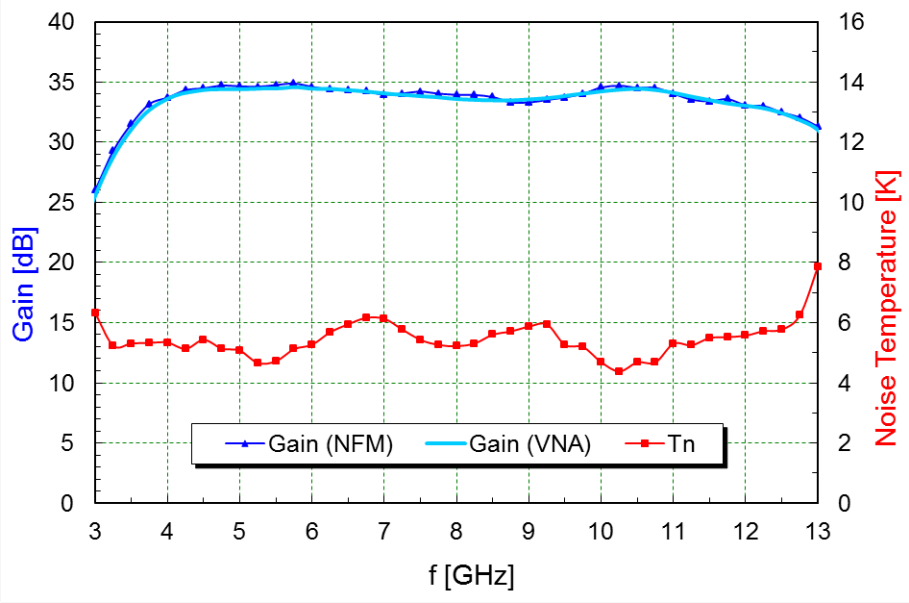

Figure 13. Gain and noise temperature plots of the X-band LNA at 14 Kelvin ambient temperature.

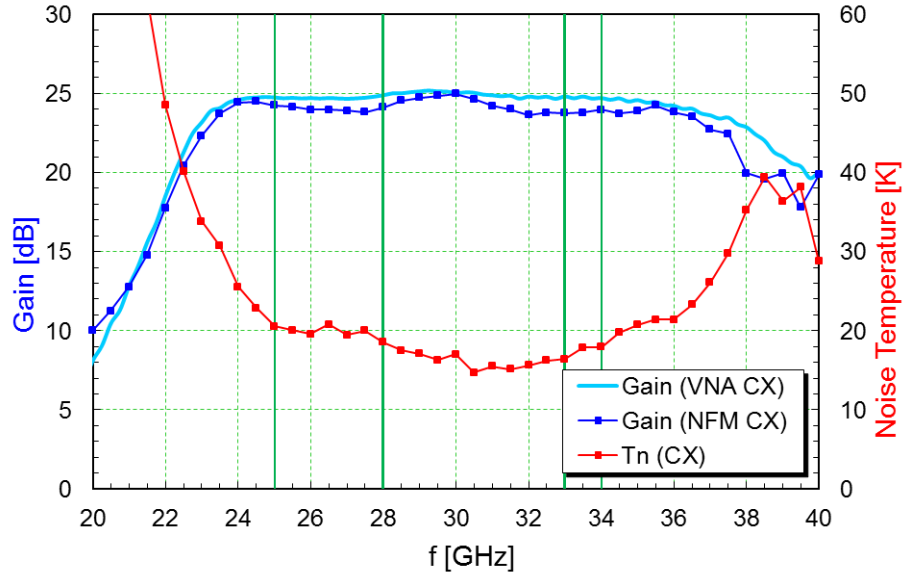

Figure 14. Gain and noise temperature plots of the Ka-band LNA at 14 Kelvin ambient temperature.

Parameter	S-band	X-band	Ka-band
Frequency range	2.2 - 2.7 GHz	7.5 - 9 GHz	28 - 33 GHz
First local oscillator	1.7 GHz	10..13 GHz	15..20 GHz
Second local oscillator	-	19.25 GHz	12.25 GHz
Output frequency range	500 - 1000 MHz	100 - 1000 MHz	500 - 1000 MHz
Gain	11.8 .. 31 dB	12.2 .. 31 dB	11.3 .. 31 dB
Po1dB	3 dBm	1 dBm	0 dBm
Input return loss	< -15 dB	< -20 dB	< -13 dB
Output return loss	< -11 dB	< -21 dB	< -11 dB

Table 4. Summary of downconverter parameters.

Preprints (www.preprints.org) | NOT PEER-REVIEWED | Posted: 31 December 2019 doi:10.20944/preprints201912.0408.v1

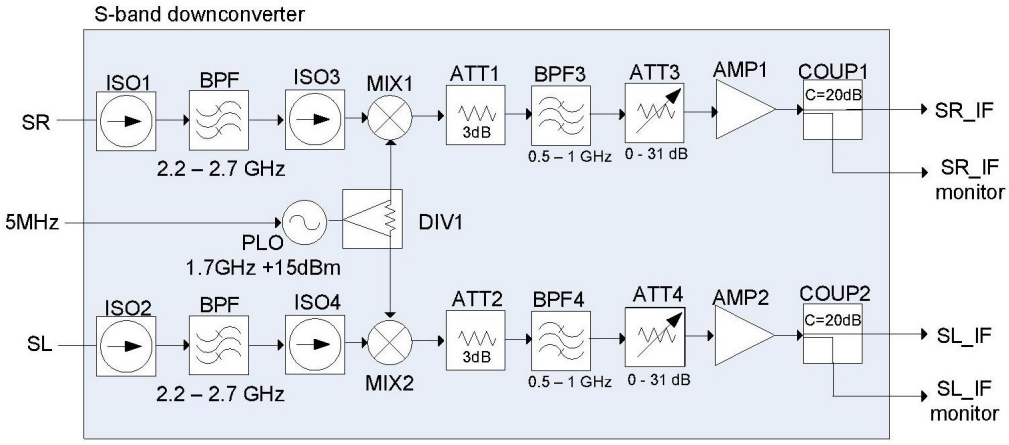

Figure 15. S-band downconverter block diagram.

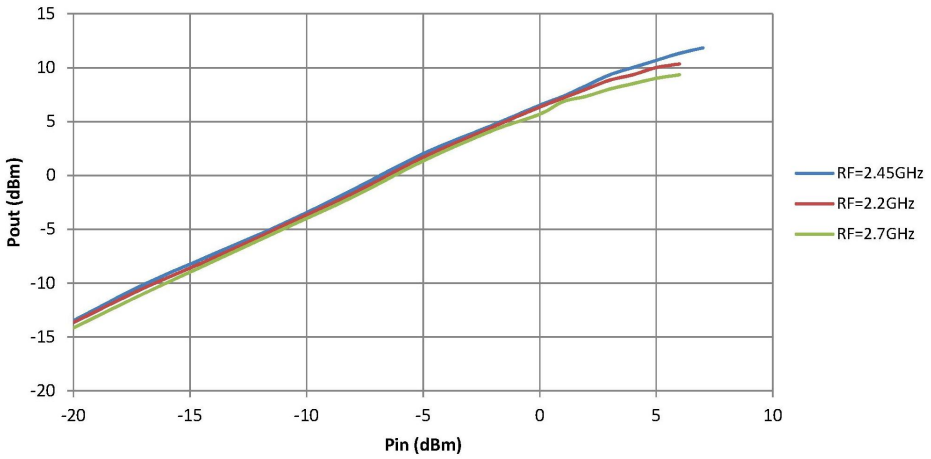

Figure 16. S-band downconverter linearity measurement.

2.6.1. S-band downconverter

The block diagram of the S-band downconverter is shown in figure 15. The whole S-band from 2.2 to 2.7 GHz is downconverter in a mixer to 500 - 1000 MHz, with the help of a phase-locked dielectric resonator oscillator (PLDRO) a 1.7 GHz. This type of LO is chosen due to its good spectral purity. Band-pass filters for image rejection are installed prior to the conversion and, after this, the final IF bandwith is limited by a 500 - 1000 MHz band-pass filter. The level of the output signal can be remotelly controlled with the help of a variable attenuator. An additional monitoring output is provided for diagnosis or connection to other backends.

Figure 16 shows the results of the linearity measurements of one of the S-band downconverter channels. The other channel is quite similar. From this figure, the Po1dB given in table 4 is obtained.

2.6.2. X-band downconverter

The block diagram of the X-band downconverter is shown in figure 17. In opposition to the S-band downconverter, designed with a single mixing stage, the X-band one has two mixing stages in an up/down conversion configuration. The first local oscillator is a frequency synthesizer in 10 - 13 GHz range. With the help of this synthesizer, any 900 MHz band width selected in the range 7.5 - 9 GHz is up-converted to 19.35 - 20.25 GHz. Later, a 19.25 GHz PLDRO allows the downconversion to 100 - 1000 MHz. The final bandwidth of the X-band converter is larger (900 MHz vs. 500 MHz) to allow for extended X-band operation.

Preprints (www.preprints.org) | NOT PEER-REVIEWED | Posted: 31 December 2019 doi:10.20944/preprints201912.0408.v1

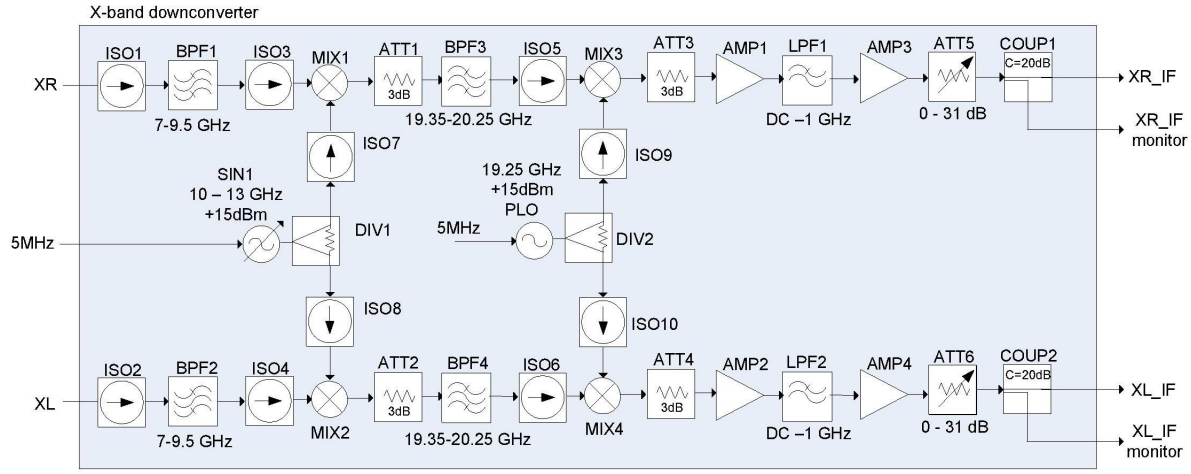

Figure 17. X-band downconverter block diagram.

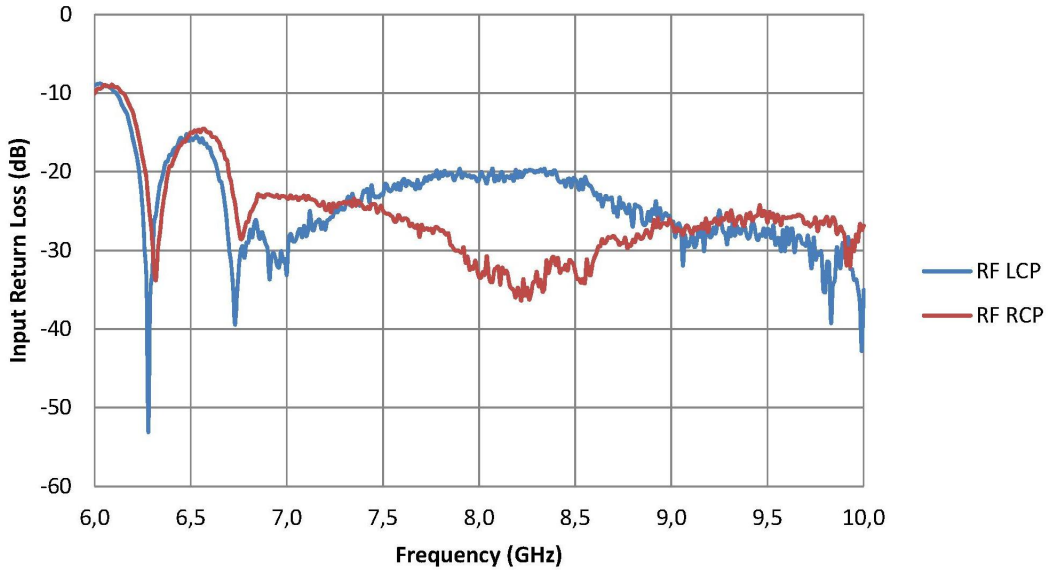

Figure 18. X-band downconverter input return losses.

Figure 18 shows the results of the input return loss measurements of the X-band downconverter. It can be seen that the return loss, in the band of interest, is lower than -20 dB in both channels.

2.6.3. Ka-band downconverter

The block diagram of the Ka-band downconverter is shown in figure 19 and figure 20 shows the downconverter itself, after integration. As in the case of the X-band downconverter, the Ka one has two mixing stages in an up/down conversion configuration. The first local oscillator is a frequency synthesizer in 15 - 20 GHz range. With the help of this synthesizer, any 500 MHz band width selected in the range 28 - 33 GHz is up-converted to 12.75 - 13.25 GHz. Later, a 12.25 GHz PLDRO allows the downconversion to 500 - 1000 MHz.

Figure 21 shows the spectrum of the LHCP channel output signal of this downconverter, for different values of the synthesizer and attenuation, when it is fed with an additive white gaussian noise source. The spectra of the output signal (500 - 1000 MHz) have been frequency shifted to the input frequency range for representation.

Preprints (www.preprints.org) | NOT PEER-REVIEWED | Posted: 31 December 2019 doi:10.20944/preprints201912.0408.v1

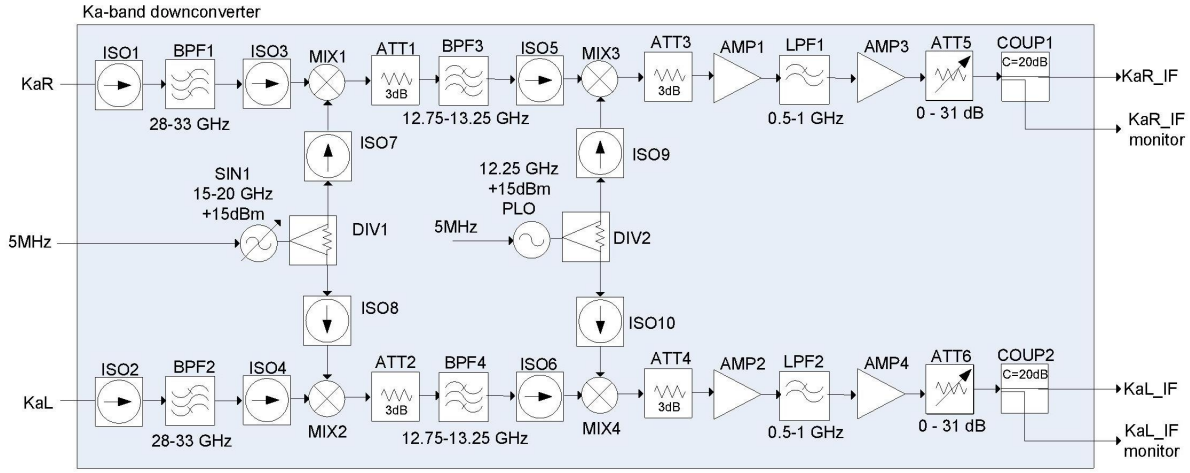

Figure 19. Ka-band downconverter block diagram.

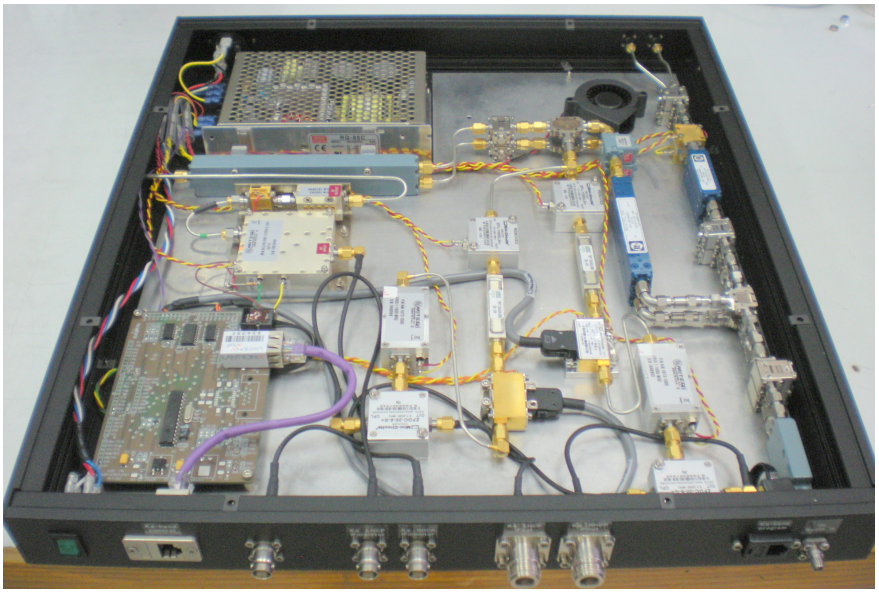

Figure 20. Ka-band downconverter.

Preprints (www.preprints.org) | NOT PEER-REVIEWED | Posted: 31 December 2019 doi:10.20944/preprints201912.0408.v1

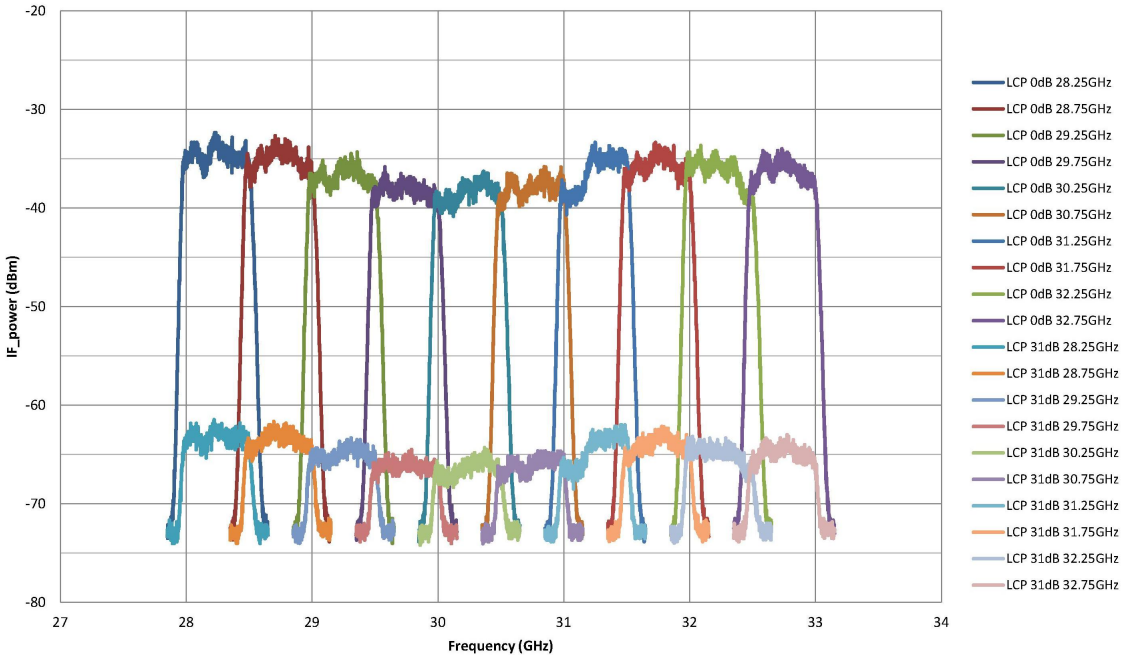

Figure 21. Ka-band downconverter spectrum.

2.7. Noise and Phase Calibration

The block diagram of the noise and phase calibration module is shown in figure 22. It contains two noise sources, a common one for both S and X bands and another for Ka-band. These diodes can be turned ON, OFF or at 80 Hz rate remotelly. The signals from each source are combined with the train of pulses from the phasecal antenna unit and then splitted for injection in each receiver channel.

The phase calibration signal is generated with the help of ultra-fast logic gates fed with 5 MHz signal from the phase calibration ground unit, following a similar aproach to that shown in [16]. Figure 23 shows the board developed in Yebes laboratories for phasecal signal generation during tests.

2.8. Receiver control

The monitoring and control of the parameters of each receiver module is performed with the help of a board developed in Yebes laboratories, too. It contains a microcontroller running at 20 MHz clock (low enough to avoid RFI), and some peripheral devices for analog and digital input/output which are controlled through inter-integrated circuit (I2C) bus. The microcontroller runs a firmware, compiled in C language, which can be easily updated through an in-circuit serial programming (ICSP) port. The microcontroller receives and sends commands from the observation computer through an ethernet adapter integrated in the board. Figure 24 shows one of these boards.

2.9. Receiver installation in the radio telescope

This section describes the mechanical installation of the receiver inside the feed cone of the 13.2 meter ring-focus radio telescope.

2.9.1. Receiver installation

The receiver is placed on a trolley with two sets of wheels that can be move along a railway system (see figure 25). On the front side of the receiver trolley, there is a flange with four precision holes for alignment. On the rear side there is a structure with two other precision holes for alignment and fixing.

The trolley with the receiver is pushed through the railway system to the end of the feed cone. The end flange of the cone has several precision pins for alignment that engage with the precision

Preprints (www.preprints.org) | NOT PEER-REVIEWED | Posted: 31 December 2019 doi:10.20944/preprints201912.0408.v1

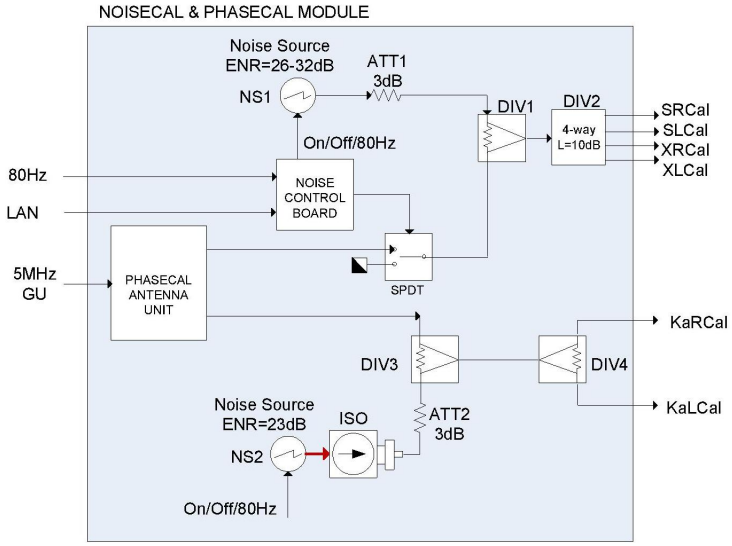

Figure 22. Calibration module block diagram.

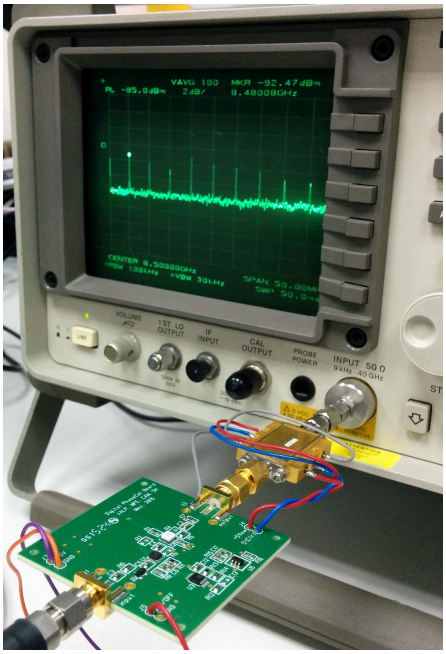

Figure 23. Phasecal generator board under tests.

Preprints (www.preprints.org) | NOT PEER-REVIEWED | Posted: 31 December 2019 doi:10.20944/preprints201912.0408.v1

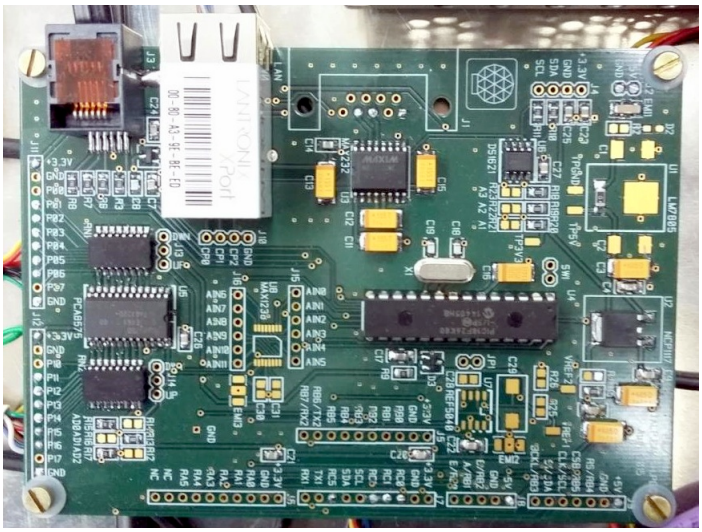

Figure 24. Control board.

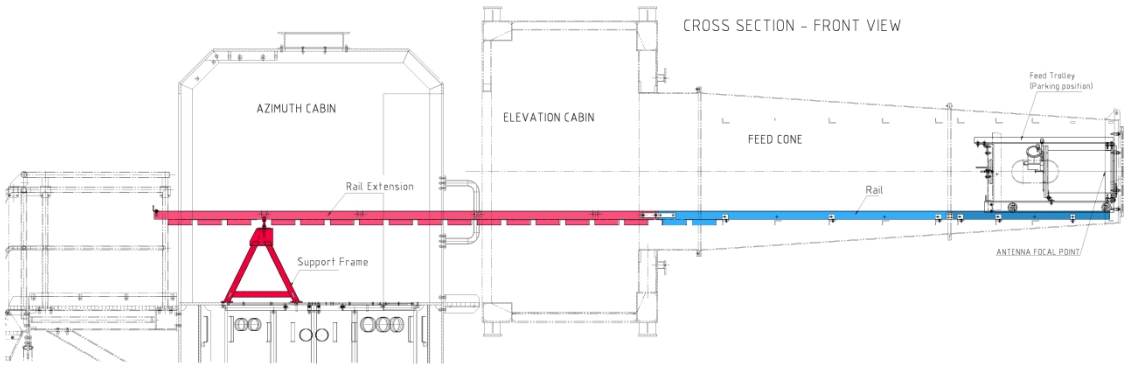

Figure 25. Railway system for receiver installation.

holes at the front of the trolley. The cone has also two precision pins in an intermediate locations, coinciding with the holes at the rear side of the trolley when it is in its final position. Those two pins have a threaded part where a special nut is screwed, fixing the trolley and avoiding any play. A railway section has been permanently installed at the feed cone for the displacement of the trolley along its length (blue rails in figure 25).

Before the installation jobs, the elevation cabin is moved to its horizontal position. Then, a second railway section is temporally installed from the balcony of the azimuth cabin to the edge of the feed cone at the elevation cabin, crossing the cabins through their doors (red rails in figure 25). This section is joined to the fix section at the cone with screws, and it rests on a support frame placed in the azimuth cabin.

Once the whole railway system is ready, the trolley is lifted from the ground level to the balcony, as shown in figure 26.

2.9.2. Conditioning of the elevation cabin

The elevation cabin was supplied with neither air conditioning nor thermal insulation. Only the feed cone was supplied with thermal insulation. The elevation cabin has been insulated using the same insulated layer than other antenna areas, and an air conditioning machine has been installed for thermal conditioning.

The air conditioning machine was selected to fit two conditions. It must operate in any position of the elevation cabin, so the water condensation in the evaporator is always correctly collected and drained outside. In addition, it must restart automatically in case of a power supply failure. The

 doi:10.20944/preprints201912.0408.v1

Figure 26. Receiver lift.

condensator has been placed at the balcony of the azimuth cabin. The electrical connection between them was laid through the elevation cable chain. The pipes were laid as described in the next section.

2.9.3. Helium and air conditioning pipes

Helium pipes for the receiver's cryogenic system and the elevation cabin air conditioning have been laid from the elevation cabin to the balcony of the azimuth cabin, where both compressors are installed. The helium compressor is not suitable for outdoor environment and has been protected into a hut provided with electrical sockets and lighting.

2.9.4. Feed cone membrane ventilation

A ventilation system has been installed to prevent water condensation on both the dewar windows and the internal side of the feed cone window. An industrial fan takes in air at the beginning of the feed cone and blows it into a duct that drives the air to the end of the cone. There, it is exhausted through a nozzle installed between both surfaces. The nozzle is fixed to the end flange of the cone, just over the trolley. The system does not interfere with the receiver trolley, which can move without any obstacle along the railways.

Figure 27 shows the setup of this ventilation system.

3. Receiver Performance

This section shows the results of the tests carried out on the tri-band receiver in the laboratory in order to check its performance.

3.1. Receiver noise and calibration temperatures

The receiver noise temperature, T_{RX}, was measured in each band using the Y-factor method, with microwave absorber submerged in liquid nitrogen (77.3 Kelvin) as cold load. The hot load was a piece of the same type of absorber at monitored room temperature. These loads were placed alternatively in front of the criostat window to proceed with the measurements. The results are shown in figures 28, 29

Preprints (www.preprints.org) | NOT PEER-REVIEWED | Posted: 31 December 2019 doi:10.20944/preprints201912.0408.v1

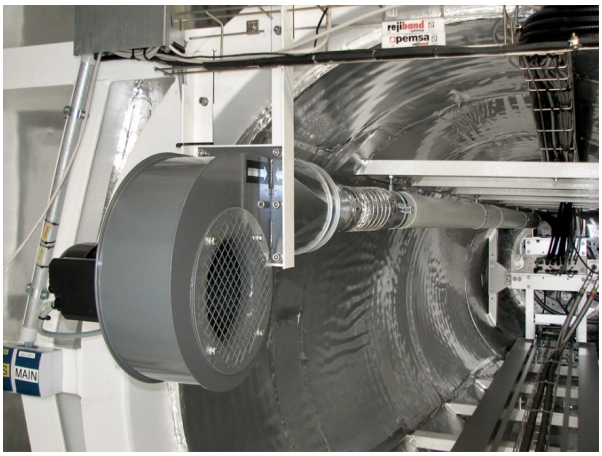

Figure 27. Fan and ducts for feed cone membrane ventilation.

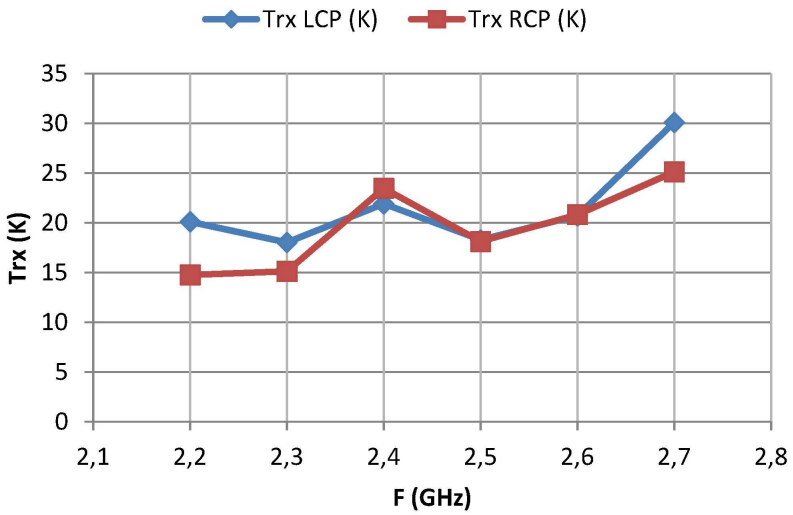

Figure 28. S-band receiver noise temperature.

and 30. It must be mentioned that in figure 28, the receiver noise increases at 2.4 and 2.7 GHz due to the existence of RFI.

The average receiver noise temperature for each band is shown in table 5, together with the average receiver calibration temperature, T_{cal}, which is the excess of noise added to the receiver by the noise diodes when they are ON (section 2.7). It was measured with the Y-factor method too, and the new T_{RX} value was substracted from the previous measurements to get the added noise from the diodes. It must be noted that the output power of the noise diodes was attenuated to get T_{cal} values about 5% of T_{RX}.

Frequency Band	**LHCP** T_{RX} (Kelvin)	**RHCP** T_{RX} (Kelvin)	**LHCP** T_{cal} (Kelvin)	**RHCP** T_{cal} (Kelvin)
S (2.2 - 2.7 GHz)	21.5	19.6	0.8	0.9
X (7.5 - 9 GHz)	22.9	22.5	1.2	1.3
Ka (28 - 33 GHz)	25.0	24.6	1.6	1.6

Table 5. Average noise receiver temperatures.

Preprints (www.preprints.org) | NOT PEER-REVIEWED | Posted: 31 December 2019 doi:10.20944/preprints201912.0408.v1

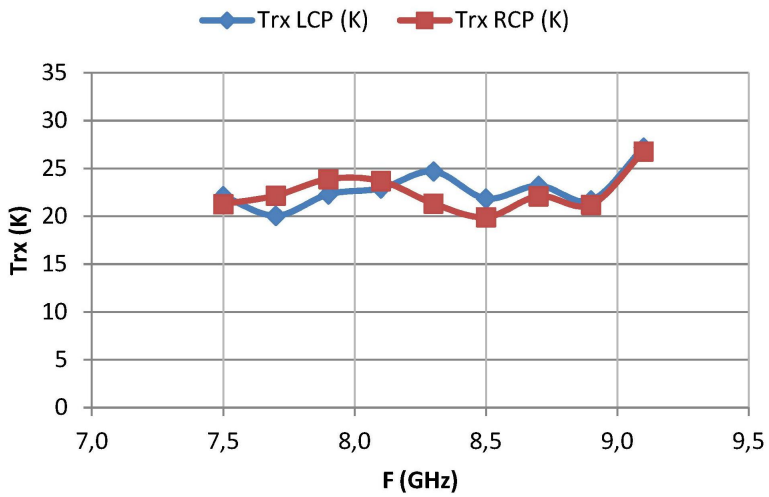

Figure 29. X-band receiver noise temperature.

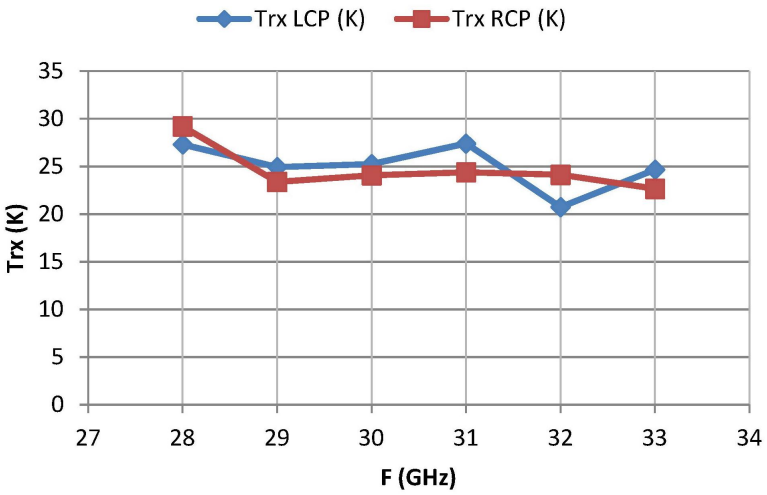

Figure 30. Ka-band receiver noise temperature.

Preprints (www.preprints.org) | NOT PEER-REVIEWED | Posted: 31 December 2019 doi:10.20944/preprints201912.0408.v1

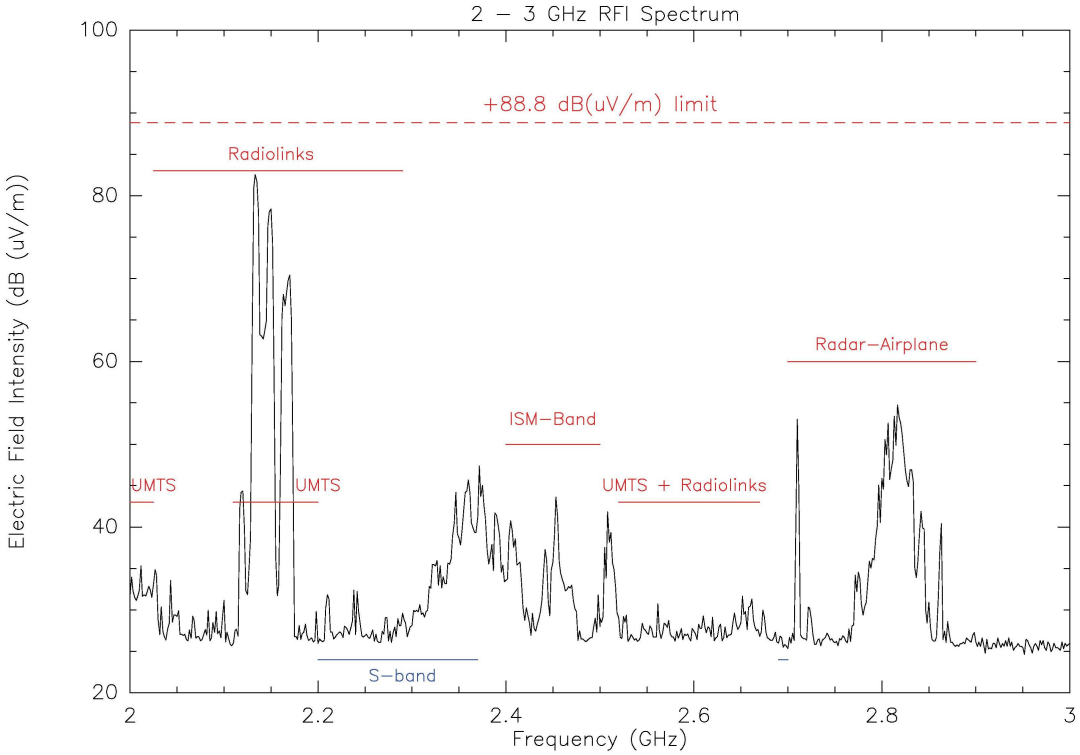

Figure 31. S-band RFI spectrum in Yebes observatory.

3.2. *Radio-Frequency Interferences (RFI)*

Radio frequency interference signals were quickly detected, due to the high sensitivity of the tri-band receiver, particularly in S-band. This is because there are several telecommunications services allocated in this band.

A detailed analysis of the RFI spectrum in Yebes observatory was carried out with the help of the RFI measurement system on the roof of the laboratory building [17]. The results of this analysis for S-band are shown in figure 31. Several RFI signals can be seen in the receiver band of interest (2.2 - 2.7 GHz). The legacy S-band for VLBI is outlined in blue (2.2 - 2.37 GHz) where some RFI signals are present too.

As a result, it is foreseen to install RFI filters in the 2.2 - 2.37 GHz band to reject RFI as much as possible. These filters where developed in a high-temperature superconducting substrate, as described in [18], and they will be installed in a future receiver upgrade.

4. Radio Telescope Performance with tri-band receiver

The radio telescope aperture efficiency, the system equivalent flux density (SEFD), system noise (T_{sys}) and half-power beam width (HPBW) were measured by radiometric means with the tri-band receiver. Table 6 and figure 32 show the results of these measurements.

Frequency Band	Efficiency (%)	SEFD (Jy)	T_{sys} (Kelvin)	HPBW (arcmin)
S (2.2 - 2.7 GHz)	70	1700	50	42.5
X (7.5 - 9 GHz)	75	1300	40	11.3
Ka (28 - 33 GHz)	60	4000	100	3.2

Table 6. Radio telescope performance parameters.

Radio telescope beam maps using Venus and 3C84 were measured too. These can be seen in figure 33, for X and Ka-bands in both circular polarization.

Preprints (www.preprints.org) | NOT PEER-REVIEWED | Posted: 31 December 2019 doi:10.20944/preprints201912.0408.v1

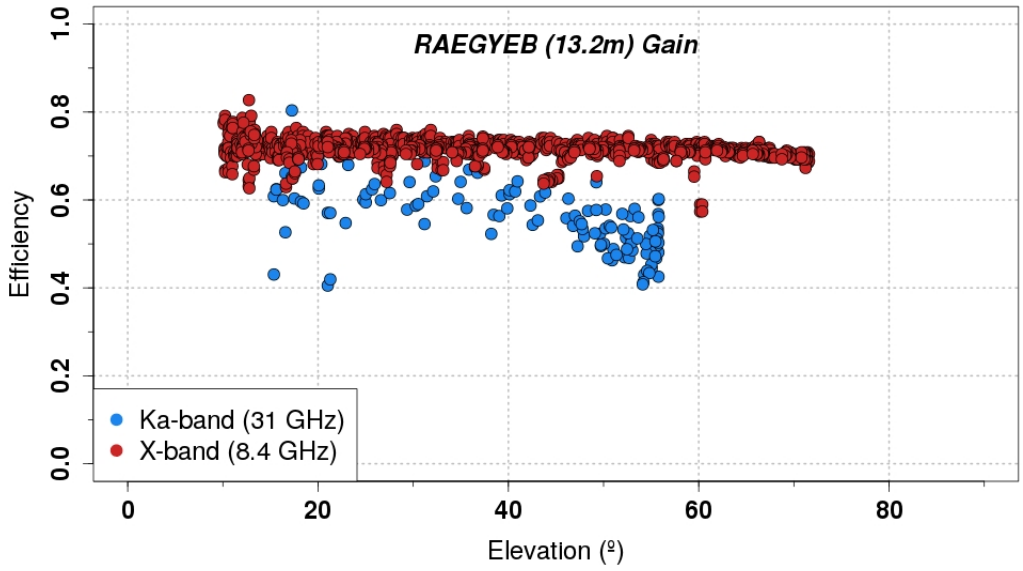

Figure 32. Aperture efficiency of 13.2 meter radio telescope in X and Ka bands.

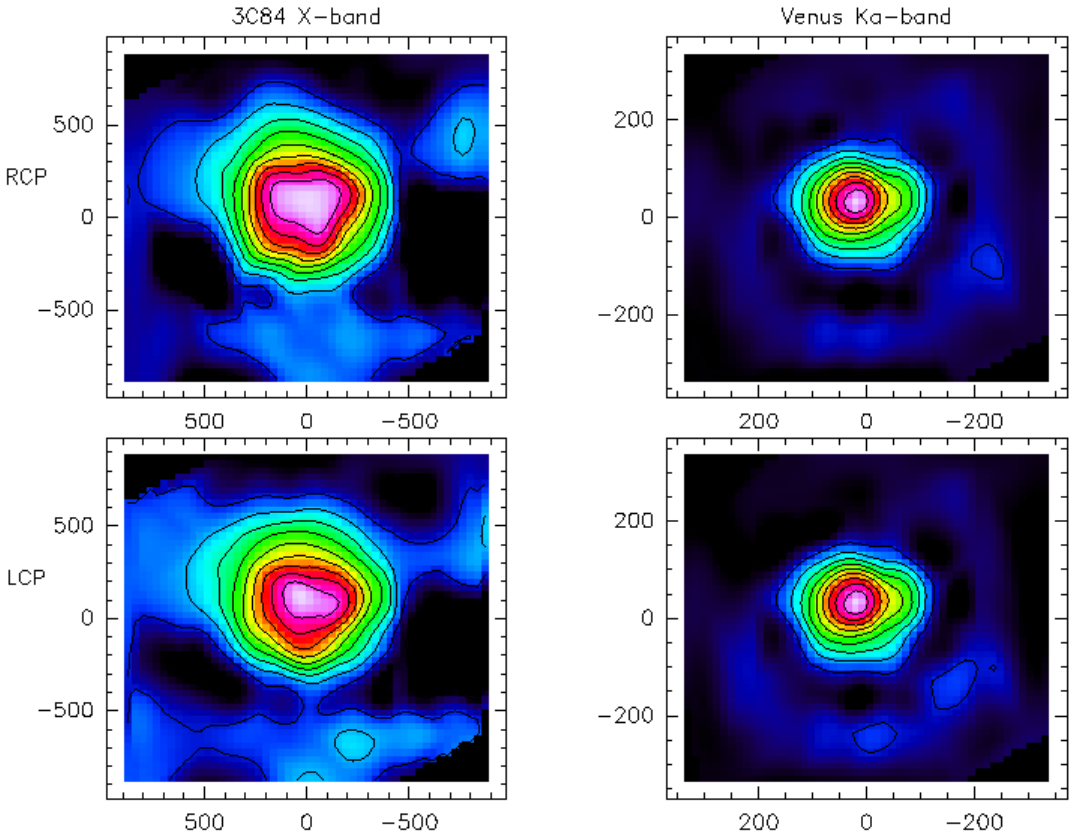

Figure 33. Radio telescope beam maps in X and Ka bands using 3C84 and Venus, respectively, for each circular polarization (RHCP and LHCP).

 doi:10.20944/preprints201912.0408.v1

5. Initial VLBI fringe tests

The tri-band receiver and the Yebes VGOS radio telescope detected VLBI fringes for the first time in November 2014, during experiment R4663 in X-band in the IVS network. Later, fringes in both S and X-bands were detected in experiments R1675, R1677, R1678, R1679 and R1680. Fringes in Ka-band where detected in 2015, too.

Experiment R1675 provided the first coordinates for the Yebes 13.2-m VGOS radio telescope.

6. Conclusions and Outlook

The technical staff of Yebes Observatory laboratories, in Spain, has developed a simultaneous tri-band (S: 2.2 - 2.7 GHz, X: 7.5 - 9 GHz and Ka: 28 - 33 GHz) low-noise cryogenic receiver for geodetic Very Long Baseline Interferometry (geo-VLBI).

The receiver was installed in the first radio telescope of the RAEGE network, which is located in Yebes Observatory, in the frame of VGOS project. After this, the receiver was borrowed by NMA for the commissioning of two VGOS radio telescopes in Ny-Alesund (Svalbard).

A second identical receiver was built for Ishioka VGOS station of GSI (Japan), and a third one for the second RAEGE VGOS station, located in Santa María (Açores archipelago, Portugal).

The average receiver noise temperatures are 21, 23 and 25 Kelvin in S-band, X-band and Ka-band, respectively, and the measured antenna efficiencies are 70%, 75% and 60% in these three bands.

This type of receivers have proven to be very usefull for the commissioning of VGOS radio telescopes, due to their high-frequency channel (28-33 GHz), and for initial VLBI tests, because they are backward compatible with legacy VLBI stations.

Now, the receiver development activities at Yebes Observatory are focused in broad-band (2-14 GHz) receivers, and associated instrumentation, for VGOS project.

Funding: This work was supported by the Spanish *Ministerio de Economía y Competitividad* under project FIS2012-38160.

Acknowledgements

The authors wish to acknowledge the assistance provided by Carlos Almendros and Sergio Henche in the receiver integration process, José A. Abad and José M. Yagüe in the construction of mechanical parts for the receiver, Joaquín Fernández in the installation of the receiver and Rafael García and Gonzalo Martínez in the assembly of low-noise amplifiers and hybrids.

Author Contributions:

José A. López-Pérez, the technical coordinator of the receiver's laboratory at Yebes, was the system engineer. He was responsible for RFI measurements too, and for the compilation of the contributions to this paper. Félix Tercero, head of antenna feed developments, and Óscar García were responsible for the design, manufacturing and tests of the tri-band feeds and Ka-band septum polarizer and coupler. Juan D. Gallego, head of LNA laboratory, Isaac López, Carmen Díez and Inmaculada Malo were responsible for LNAs and microwave hybrid couplers' design, manufacturing and tests. María Patino and Pablo García were responsible for downconverters' and calibration modules design, construction and tests and hardware for receiver control. José A. López-Fernández, Deputy Director of Astronomy, Geophysics and Space Applications, José M. Serna and Beatriz Vaquero were responsible for the dewar development and vacuum and cryogenic tests. Pablo de Vicente, Director of Yebes Observatory, Laura Barbas and F. J. Beltrán, were responsible for telescope and receiver control software and telescope performance tests. Javier González was responsible for VLBI backends, fringe tests and observations. Carlos Albo was responsible for receiver installation and telescope servos.

Conflicts of Interest:

The authors declare no conflict of interest.

Abbreviations

The following abbreviations are used in this manuscript:

ESD	Electrostatic Discharge
GSI	Geospatial Information Authority of Japan
HPBW	Half-Power Beam Width
I2C	Inter-Integrated Circuit
ICSP	In-Circuit Serial Programming
IGN	Instituto Geográfico Nacional
IVS	International VLBI Service
LNA	Low Noise Amplifier
NMA	Norwegian Mapping Autorithy
RAEGE	Red Atlántica de Estaciones Geodinámicas y Espaciales
RFI	Radio Frequency Interference
SEFD	System Equivalent Flux Density
VGOS	VLBI Global Observing System
VLBI	Very Long Baseline Interferometry

1. Hase, H.; Behrend, D.; Ma, C.; Petrachenko, B.; Schuh, H.; Whitney, A. The Emerging VGOS Network of the IVS. *Progress Report of the IVS, VLBI2010 Committee*, **2010**.
2. Gómez, J.; Colomer, F.; López Fernández, J.A.; Assis, M.C.S. RAEGE: An Atlantic Network of Geodynamical Fundamental Stations. *IVS 2010 General Meeting Proceedings* pp. 101-105, Hobart, Australia, **2010**.
3. López-Pérez, J. A.; Tercero, F.; Serna, J. M.; López-Fernández, J. A. A Tri-band Cryogenic Receiver for the RAEGE Project Antennas. *Proceedings of the 7th IVS General Meeting*, Madrid, Spain, March 4-9, **2012**.
4. Kildal, P.-S.; Yang, J.; Karandikar, Y.; Wadefalk, N.; Pantaleev, M.; Helldner, L. Development of a coolable 2-14 GHz Eleven feed for future radio telescopes for SKA and VLBI 2010. **2009** *International Conference on Electromagnetics in Advanced Applications*, pp. 545-547.
5. Akgiray, A.;Weinreb, H. S.; Imbriale, W. A.; and Beaudoin, B. Circular Quadruple-Ridged Flared Horn Achieving Near-Constant Beamwidth Over Multioctave Bandwidth: Design and Measurements. *IEEE Trans. on Ant. and Prop.*, **2013** *Vol. 61, Issue 3*, pp. 1099 - 1108.
6. Cortés-Medellín, G.; Non-Planar Quasi-Self-Complementary Ultra-Wideband Feed Antenna. *IEEE Transactions on Antennas and Propagation*, **2011**, *vol. 59, no. 6*, .
7. García, E.; Llorente-Romano, S.; García-Lampérez, A.; Javier-Herraiz, F.; Salazar-Palma, M.; Segovia-Vargas, D.; Serna, J.M.; Tercero, F.; López-Pérez, J.A.; Colomer, F.; López-Fernández, J.A. Dyson conical quad-spiral array as ultrawideband feed system. *36th ESA Antenna Workshop, ESTEC*, 8-Oct-2014.
8. Malo, I.; Gallego, J.D.; Díez, C.; López-Fernández, I.; Briso, C. Cryogenic Hybrid Coupler for Ultra-Low-Noise Radio Astronomy Balanced Amplifiers. *IEEE Trans. Microw. Theory Tech., vol. 57, no. 12*, **2009**.
9. Shimizu, J.K.; Jones, E.M.T. Coupled-transmission-line directional couplers. *IRE Trans. Microw. Theory Tech., vol. 6*, **1958**, pp. 403-410.
10. López-Fernández, I; Gallego, J. D.; Diez, C.; Barcia, A.; Pintado, J. M. Wide Band, Ultra Low Noise Cryogenic InP IF Amplifiers for the Herschel Mission Radiometers. *Millimeter and Submillimeter Detectors for Astronomy, Proc. SPIE, vol. 4855, pp. 489-500*, **2003**.
11. López-Fernández, Isaac; Gallego-Puyol, Juan D.; Diez-González, Carmen; Barcia-Cancio, Alberto. Development of Cryogenic IF Low Noise 4-12 GHz Amplifiers for ALMA Radio Astronomy Receivers. *IEEE MTT-S Int. Microwave Symp.Dig., pp. 1907-1910, Jun.* **2006**.
12. López-Fernández, Isaac; Gallego-Puyol, Juan D.; Homan, O.J.; Barcia-Cancio, Alberto. Low Noise Cryogenic X-Band Amplifier Using Wet-Etched Hydrogen Passivated InP Devices. *IEEE Microwave Guided Wave Lett., vol. 9, pp. 413-415, Oct.* **1999**.
13. Aja-Abelán, Beatriz; Seelmann-Eggebert, Matthias; Bruch, Daniel; Leuther, Arnulf; Massler, Hermann; Baldischweiler, Boris; Schlechtweg, Michael; Gallego-Puyol, Juan D.;López-Fernández, Isaac; Diez-González, Carmen; Malo-Gómez, Inmaculada; Villa, Enrique; Artal, Eduardo. 4-12 GHz and 25-34 GHz Cryogenic mHEMT MMIC Low-Noise Amplifiers. *IEEE Transactions on Microwave Theory and Techniques, vol. 60, pp 4080-4088, Dec.* **2012**.

14. Gallego-Puyol, Juan D.; López-Fernández, Isaac; Diez-González, Carmen. A Measurement Test Set for ALMA Band 9 Amplifiers. *RadioNET FP7 1st Engineering Forum Workshop: Low Noise Figure Measurements at Cryogenic and Room Temperature, Chalmers University of Technology, April* **2009**.
15. Gallego-Puyol, Juan D.; Cano, Juan L. Estimation of Uncertainty in Noise Measurements Using Monte Carlo Analysis. *RadioNET FP7 1st Engineering Forum Workshop: Low Noise Figure Measurements at Cryogenic and Room Temperature, Chalmers University of Technology, April* **2009**.
16. Rogers, A.E.E. Preliminary circuit for the new phase cal. *Mark 5 memo nr. 75*, **2008**, Massachusetts Institute of Technology, Haystack Oservatory, Westford, Massachusetts 01886.
17. López-Pérez, J. A.; López-Fernández, J. A. First Radio-Frequency Interference Measurement Campaing at Yebes Observatory. *Yebes Observatory Internal Technical Report, IT-OAN-2010-5*, **2010**.
18. Huang, F.; Bolli, P.; Cresci, L.; Mariotti, S.; Panella, D.; López-Pérez, J. A.; García-Carreno, P. Superconducting spiral bandpass filter designed by a pseudo-Fourier technique. *IET Microwaves, Antennas and Propagation, vol. 12, Iss. 8, pp. 1293-1301,* **2018.**